HHS Public Access

Author manuscript

Biomater Sci. Author manuscript; available in PMC 2022 February 23.

Published in final edited form as:

Biomater Sci. 2021 February 23; 9(4): 1363–1373. doi:10.1039/d0bm01815e.

Responsive hyaluronic acid-gold cluster hybrid nanogel theranostic systems

Ying Lin[a], **Chen Li**[b], **An Liu**[a], **Xu Zhen**[b], **Jiangang Gao**[a], **Wei Wu**[b], **Weibo Cai**[c], **Xiqun Jiang**[b]

[a]Anhui Laboratory of Functional Coordinated Complexes for Materials Chemistry and Application, College of Biological and Chemical Engineering, Anhui Polytechnic University, Wuhu 241000, P. R. China.

[b]MOE Key Laboratory of High Performance Polymer Materials and Technology, and Department of Polymer Science & Engineering, College of Chemistry & Chemical Engineering, Nanjing University, Nanjing, 210093, P. R. China.

[c]Department of Radiology, University of Wisconsin-Madison, Madison, WI 53705, USA

Abstract

Tumor microenvironment responsive and self-monitored multimodal synergistic theranostic strategies can significantly improve therapeutic efficacy by overcoming biological barriers. Herein, we report a type of smart fluorescent hyaluronic acid nanogel that can respond to the reducing microenvironment and activate tumor targeting with light-traceable monitoring in cancer therapy. First, the derivative of hyaluronic acid (HA) with a vinyl group and cystamine bisacrylamide were used to synthesize bioreducible HA based nanogels *via* copolymerization in aqueous medium. Then, multifunctional mHA-gold cluster (mHA-GC) hybrid nanogels were successfully prepared by the *in situ* reduction of gold salt in the HA nanogels. The HA matrix turns the nanogels into a capsule for effective drug loading with excellent colloidal stability. Interestingly, the reducing tumor microenvironment dramatically enhanced the fluorescence signal of gold clusters in the hybrid nanogels. The highly selective cancer cell uptake and efficient intratumoral accumulation of the hybrid nanogels were demonstrated by fluorescence tracking of these nanogels. Responsive disassembly of the hybrid nanogels and drug release were triggered by excess glutathione presence in cancer cells. Moreover, *in vivo* and *in vitro* tumor suppression assays revealed that the doxorubicin-loaded hybrid nanogels exhibited significantly superior tumor cell inhibition abilities compared to free DOX. Overall, the mHA-GC hybrid nanogels emerge as a promising theranostic nanoplatform for the targeted delivery and controlled release of antitumor drugs with light-traceable monitoring in cancer treatment.

Introduction

Nanotechnology based tumor imaging has rapidly developed in recent years, especially, imaging-guided chemotherapy.[1–3] However, anticancer drugs are often insufficient to cause

liny@ahpu.edu.cn, jiangx@nju.edu.cn.

Conflicts of interest

There are no conflicts of interest to declare.

tumor regression and eradication due to the absence of selectivity to tumors and tumor cells, leading to low drug concentration at the tumor sites and severe side effects.[4,5] The application of nanoscale drug delivery systems offers a potential solution for current challenges in cancer therapy. In order to enhance the accumulation in the tumor and intratumoral drug release, various nanomedicines have been developed and applied by virtue of their tunable physicochemical properties, including their shape, size, surface charge, targeting moiety and functional groups.[6–8] Nevertheless, the *in vivo* antitumor activity of many designed nanocarriers has not been as high as initially envisioned due to the complexity of the tumor vascular system and premature drug release in the blood circulation.

For the proper negotiation of the biological barriers, a large number of investigations are being continually carried out into the integration of innovative design features within nanocarrier constructs to create multifunctional nanoparticulate systems. Oftentimes, the stimulus response is an important feature of these systems. It has been demonstrated that drug release could be triggered from “smart” nanocarriers by various endogenous stimuli, including temperature, pH, enzymes, and redox and hypoxic surroundings, in passive or active targeting systems.[9–12] Among the responsive systems, glutathione (GSH) has been considered as an ideal reductive trigger for controlled drug delivery because of its more than 10-fold higher levels in cancer lesions than in normal cells.[13,14]

Another widely used strategy to improve the therapeutic efficacy of nanomedicine is receptor-mediated cancer cell uptake. CD44 and CD168 (also called the receptor for hyaluronan mediated motility, RHAMM) are over-expressed on the surface of various malignant tumor cells. Both can selectively bind hyaluronic acid (HA), a natural polysaccharide that is a major constituent of the extracellular matrix and synovial fluid.[15–17] HA has several advantageous features for biomedical applications, such as biocompatibility, anti-adhesivity, biodegradability and non-immunogenicity.[18] Thus, as an optimal ligand, HA has been extensively exploited in targeted drug delivery and cancer therapeutics. Recently, HA-containing hydrogels and conjugates have been widely studied, and they can also be used as the targeting ligands for the delivery of other nanoprobes, DNA and siRNA.[15,19,20] The integration of hyaluronic acid and fluorescent probes for monitoring the release of drugs and the recognition of tumor cells provides numerous advantages. Gold nanoclusters are an ideal type of luminescent probe due to their low toxicity and size-dependent fluorescence properties.[21–23] Moreover, gold nanoclusters are different from the nanoparticles as they exhibit molecular-like properties, good photostability and long-lifetime fluorescence in the near-infrared region, which makes them highly suitable for *in vitro* and *in vivo* imaging.[24] Given these advantages, the incorporation of gold clusters and drugs within redox responsive HA-based nanogels will generate a synergistic anticancer effect with bioimaging function.

In this study, we aimed to develop a novel type of multifunctional hyaluronic acid nanogel by encapsulating gold clusters and DOX for combined diagnosis and therapy. As shown in Scheme 1, methacrylated hyaluronic acid (mHA) was initially synthesized, and then copolymerized with disulfide-containing cystamine bisacrylamide (CBA) to produce reducible mHA nanogels. The gold cluster-encapsulated mHA hybrid nanogels were prepared by loading gold salt, followed by *in situ* reduction of the gold salt in aqueous solution. The high density of carboxylic acid groups in the hyaluronic acid molecule endows

the hybrid nanogels with high stability in saline and enables the nanogels to effectively load a positively charged drug *via* electrostatic interaction. Meanwhile, the HA component endows the nanogels with excellent target ability toward tumor tissues by both passive and active targeting. In addition, due to the existence of disulfide linkages, the mHA-gold cluster (mHA-GC) nanogels would readily be disassembled in response to the reductive environment, especially in intracellular environments and tumor tissues where the reducing agent GSH has relatively high concentration,[13] allowing the tumor- and cytoplasm-specific release of the entrapped drug. More importantly, the fluorescence signal of the HA hybrid nanogels could increase with the increase of the GSH concentration. Therefore, the mHA-GC hybrid nanogels could not only emit the near-infrared fluorescence signal to detect the tumor area and monitor the drug delivery by using *in vivo* bioimaging but also easily release the drug to kill cancer cells under reducing conditions.

Experimental section

Materials

Sodium hyaluronic acid (M_w = 50 kDa) was obtained from Freda Biochem Co. Ltd (Shangdong China). Methacrylic anhydride and acrylyl chloride were obtained from Adamas Reagent Co. Ltd. Cystamine dihydrochloride and glutathione (GSH) were bought from Aladdin Industrial Corporation. Chloroauric acid ($HAuCl_4$) and sodium borohydride ($NaBH_4$) were supplied by Sinopharm Chemical Reagent Co. Ltd (Shanghai, China). Doxorubic hydrochloride (DOX) was purchased from Shenzhen Main Luck Pharmaceuticals Inc. (Shenzhen, China). Potassium persulfate ($K_2S_2O_8$) was recrystallized from deionized water. Dimethyl sulfoxide (DMSO) and triethylamine were distilled under reduced pressure from calcium hydride. All other reagents were of analytical grade and used without further purification. Murine hepatic H22 cell line, human pulmonary carcinoma cell line A549 and murine embryonic fibro-blast cell line NIH3T3 were provided by Shanghai Institute of Cell Biology (Shanghai, China). Male ICR mice (6–8 weeks old) were supplied by the Animal Center Laboratory of Nanjing Medical University (Nanjing, China). All animal experiments were performed in accordance with the Guidelines for Care and Use of Laboratory Animals of Nanjing University and approved by the Animal Ethics Committee of Drum-Tower Hospital.

Synthesis of methacrylated hyaluronic acid (mHA)

2 g of hyaluronic acid was dissolved in 50 mL of dry dimethyl sulfoxide, and then 3 mL of triethylamine was added. 2.5 mL of methacrylic anhydride dissolved in DMSO solution (10 mL) was subsequently added dropwise to the system under stirring. The resulting mixture was stirred at room temperature for 12 h. Thereafter, the reaction mixture was precipitated in ethanol and washed with ethanol three times. After being dried under vacuum at 30 °C, the crude product was added to 70 mL of deionized water and then the pH of the solution was adjusted to around 7 with a 1 M NaOH solution. The product was collected by precipitating in ethanol and washed with ethanol three times. Finally, the obtained mHA was dried under vacuum and characterized by ^1H NMR using D_2O as the solvent.

Synthesis of redox responsive mHA nanogels

The mHA nanogels were synthesized by the radical polymerization of mHA with CBA. Briefly, mHA (40 mg) and CBA^{25} (40 mg) were dissolved in 30 mL of deionized water by heating. After the aqueous solution became clear, the polymerization was initiated by 300 mg of $K_2S_2O_8$ at 80 °C and proceeded for 10 min under a nitrogen atmosphere. Finally, the resultant suspension was filtered and dialyzed against deionized water using a dialysis bag (MWCO: 14 kDa) to remove residual monomers and other small molecules.

Preparation of mHA-gold cluster (mHA-GC) hybrid nanogels

1.1 mL of $HAuCl_4$ solution (10 mg mL^{-1}) was dropped slowly into 10 mL of the mHA nanogel suspension under vigorous stirring. Then the pH of the mixture solution was adjusted to 10 using NaOH solution (1 mol L^{-1}). Thereafter, 0.7 mL of ice-cold $NaBH_4$ (0.012 mol L^{-1} was slowly added to the above solution under constant stirring. The solution turned light brown after stirring for 48 h. The obtained suspension was filtered and then dialyzed with a 14 kDa cutoff membrane for 48 h to remove small molecules

Characterization

Nuclear magnetic resonance (NMR) spectra were recorded using a Bruker AVANCE III HD spectrometer with tetramethyl-silane as an internal standard. Fourier transform infrared (FT-IR) spectra were recorded on a Nicolet 510p spectrometer. The hydrodynamic diameter and distribution of the nanogels were evaluated by the dynamic scattering (DLS) method using a Brookhaven BI9000 AT system and zeta potentials with a ZetaPlus instrument (Brookhaven Instruments Co., USA). All results were the average of triplicate measurements. Morphological studies of the nanogels were performed by transmission electron microscopy (TEM) (JEM-1011, JEOL) and scanning electron microscopy (SEM) (S-4800, Hitachi). The composition of gold and sulfur in the sample was estimated by using a Vario EL II elemental analyzer (Elementar). The quantification of the gold clusters in the hybrid nanogels was performed by inductively coupled plasma mass spectrometry (ICP-MS) (Agilent 7500a). The X-ray photoelectron spectroscopy (XPS) measurement was carried out with a Thermo Escalab 250XI electron spectrometer. A standard Al Kα excitation source was used. The photoluminescence (PL) spectra were collected using an RF-5301PC spectrofluorometer (Shimadzu), and UV-Vis absorption spectra were recorded with a UV-3600 spectrophotometer (Shimadzu). The slit width of the spectrofluorometer was 5 nm in both the excitation and emission monochromators. The fluorescence quantum yields were determined by comparing the integrated fluorescence intensity of the mHA-GC nanogel solutions and Rhodamine 6G in the matched absorbance region. The samples were diluted so that they were optically thin.

Cell uptake of mHA-GC hybrid nanogels

For cellular uptake examination, the A549, H22 and NIH3T3 cells were seeded into a six-well plate at a density of 2.5×10^5 cells and cultured at 37 °C in a humidified atmosphere of 5% CO_2 for 24 h. Then, 200 μL of the mHA-GC hybrid nanogels was added into each well and allowed to incubate for another 4 h. After the incubation, the cells were washed three times with PBS at 37 °C and 4 °C, respectively. The Hoechst 33258 stained cell nuclei were

observed by confocal laser scanning microscopy (CLSM) (LSM 710, Zeiss Inc., Germany). The Hoechst 33258 and gold cluster excitation was performed with a 405 nm diode laser and a 488 nm argon laser, respectively.

Flow cytometry was employed to quantify the cellular uptake. The A549, H22 and NIH3T3 cells were seeded into a six-well plate at a density of 2.5×10^5 cells and grown for 24 h, and then incubated at 37 °C for additional 4 h with the mHA-GC hybrid nanogels (200 μg mL $^{-1}$). Thereafter, the cells were washed three times with PBS and detached with a 0.25% trypsin solution. The cells were collected by centrifugation and washed with ice-cold PBS. Then, the resuspended cells were immediately scanned using a flow cytometer (BD Accuri C6, USA).

In vivo real-time fluorescence imaging

To establish the experimental tumor model, H22 cells ($4–6 \times 10^6$ H22 cells per mouse) were inoculated subcutaneously into the left armpit of male ICR mice (6–8 weeks). The mice were kept until the tumor had grown to an acceptable size. After that, the mHA-GC hybrid nanogels were intravenously injected *via* the tail vein. *In vivo* imaging of the mice was recorded at different time intervals post-injection using a MaestroTM fluorescence imaging system (CRi, Inc., USA) after anaesthesia. Once the experiment was completed, the mice were euthanized for isolated organ imaging (such as tumor, heart, liver, spleen, stomach and kidneys).

Preparation of DOX-loaded hybrid nanogels

To a stirred suspension of the hybrid nanogels in water (5 mg mL^{-1}, 4 mL), the pH of which was adjusted to 8 with NaOH solution beforehand, was added dropwise 1 mL of DOX aqueous solution. The mixed solution was stirred at room temperature for 12 h in the dark to allow DOX to diffuse into the nanogel matrix. Thereafter, the mixture was centrifuged at 12 000 rpm for 40 min to remove unloaded DOX. The sediment was redispersed in PBS, giving a suspension of DOX-loaded mHA-GC hybrid nanogels. The concentration of free DOX in the supernatant was obtained by detecting the absorbance at 480 nm based on a calibration curve, and the precipitate was weighed after vacuum drying. The drug encapsulation efficiency (DE) and drug loading (DL) content of the hybrid nanogels were calculated as follows:

$$\mathrm{DE}(\%) = \frac{M(\text{feeding drug}) - M(\text{drug in supernatant})}{M(\text{feeding drug})} \times 100\% \quad (1)$$

$$\mathrm{DL}(\%) = \frac{M(\text{feeding drug}) - M(\text{drug in supernatant})}{M(\text{drug-loaded nanospheres})} \times 100\% \quad (2)$$

In vitro GSH-triggered DOX release of the hybrid nanogels

A known amount of the DOX-loaded hybrid nanogels was transferred into a dialysis bag (MWCO = 14 kDa). The dialysis bag was then immersed in 5 mL of PBS (10 mM, pH = 7.4, 6.0 and 5.0, respectively) without or with 10 mM glutathione (GSH), and incubated at 37 °C.

At certain times, 5 mL of the outside buffer solution was taken out and 5 mL of fresh PBS was added without or with GSH at the corresponding pH value. UV-Vis spectrometry was employed to determine the amount of the released DOX by measuring the absorbance at 480 nm with a pre-established calibration curve as the reference. The results were the average of three measurements.

In vitro cell cytotoxity

The cell cytotoxicity of free DOX and the DOX-loaded mHA-GC hybrid nanogels toward the three cancer cell lines (A549, NIH3T3 and H22 cell lines) was estimated by MTT assays. Briefly, a population of 5000 cells for each cell line was seeded in a 96-well plate and incubated in 200 μL of the culture medium containing samples with various concentrations at 37 °C for 24 h in a humidified atmosphere with 5% CO_2. The samples included free DOX, the DOX-loaded hybrid nanogels and the blank mHA-GC hybrid nanogels. Each sample was repeated three times. After the incubation, the culture medium was discarded and the cells were washed twice with 4 °C PBS. Then 200 μL of fresh medium with 500 μg mL^{-1} of 3-(4,5-dimethylthiazol-2-yl)-2,5-diphenyltetrazolium bromide (MTT) was added into each well and incubated for another 4 h. After removing the medium, 150 μL per well of DMSO was used to dissolve the formazan crystals, and the absorbance of each well at 570 nm was detected on a microplate reader (Huadong, DG-5031, China). The cell viability was calculated by using the following formula:

$$\text{Cell viability}(\%) = \frac{\text{Abs(test cell)} - \text{Abs(background)}}{\text{Abs(controlled cell)} - \text{Abs(background)}} \times 100\% \quad (3)$$

Determination of cell apoptosis and proliferation

To verify the antitumor efficacy of the mHA-GC hybrid nanogels, H22 bearing mice with an acceptable size were divided into five groups containing three mice each. The groups were treated with saline, the mHA-GC hybrid nanogels, free DOX, a single injection of the DOX-loaded hybrid nanogels and multiple injections of the DOX-loaded hybrid nanogels, respectively. The tumors were excised at day 8 after injection, fixed with 10% formalin, embedded in paraffin and thereafter cut into 4 μm slices. The slices were stained by terminal deoxynucleotidyl transferase dUTP nick end labeling (TUNEL) or proliferating cell nuclear antigen (PCNA) methods, respectively. For the quantification of the TUNEL and PCNA expression, 10 random fields were chosen to calculate the percentage of the positive cells in the total cells.

Statistical analysis

All the results were expressed as means ± SD. Statistical analyses were performed using ANOVA analysis and Student's *t*-test. The results were considered statistically significant when the P value was less than 0.05.

Results and discussion

Preparation of mHA-GC hybrid nanogels

To prepare the mHA nanogels, hyaluronic acid was reacted with methacrylic anhydride to afford methacrylated hyaluronic acid (mHA). Thereafter, the mHA nanogels were obtained by copolymerization between mHA and cystamine bisacrylamide (CBA) in an aqueous solution, as shown in Scheme 1. Fig. 1A shows the ^{1}H NMR spectra of the HA before and after the incorporation of the methacrylate group. On a comparison with the spectrum of HA, the spectrum of mHA shows three peaks located 6.1, 5.8 and 2.1 ppm that can be assigned to the protons of methylene (a, b) and methyl (c), respectively, confirming the methacrylation modification of HA. The degree of substitution was determined to be 15.1% from the relative integrations of the methacrylated proton peaks into polysaccharide protons. It is worth mentioning that the peaks from the ethylene group adjacent to the methacrylate group are hardly utilizable due to the overlapping with the peaks from the HA backbone.

The FT-IR spectra of mHA, CBA and the mHA nanogels are shown in Fig. 1B. For the nanogels, the main adsorption bands at 3380 cm^{-1} for the hydroxyl group of mHA, and 1533 cm^{-1} for the N–H bond, and 1230 cm^{-1} for the C–N bond of CBA were observed, thus indicating that the nanogels were composed of mHA and CBA. The diameter of the mHA nanogels was tunable from 206 to 124 nm by changing the feeding concentration of mHA while keeping the concentrations of others unchanged, as shown in Fig. 1C. This is primarily ascribed to the decrease in the amount of polymer and the increase in the cross-linking degree within the nanogels. Also, it can be seen that the zeta potential of the mHA nanogels shows a negative value in the range of concentrations observed. To enhance the extravasation and penetration in the tumors, the mHA nanogels with a 124 nm diameter were chosen for subsequent experiments. The TEM image showed that the mHA nanogels have a spherical shape and narrow size distribution, as shown in Fig. 1D.

For the preparation of mHA-Gold cluster hybrid nanogels, the mHA nanogels were used to load gold salt, followed by *in situ* reduction of gold salt in aqueous solution, as illustrated in Scheme 1. It was observed that mixing chloroauric acid with mHA nanogels in basic solution led to a gradual fading of the light yellow color, indicating the formation of Au(I) complexes due to the interaction of gold ions with the disulfides of CBA. Then, the reducing agent $NaBH_4$ was added to reduce Au(I) into gold clusters, and the color of the solution slowly turned to light brown, suggesting the formation of the gold clusters. In this process, CBA within the mHA nanogels was employed not only to reduce Au(III) in the reaction system but also to act as a protecting agent for the gold clusters. Thus, pre-reduction was strictly confined within the mHA nanogels, endowing these nanogels with a nanosized precursor reaction system for the synthesis of mHA-GC hybrid nanogels. Obviously, this strategy guarantees that almost all of the gold clusters were immobilized within the hybrid nanogels. The obtained hybrid nanogels still showed a spherical morphology and narrow size distribution in the TEM and SEM images (Fig. 2A and B). The average size of the hybrid nanogels obtained using an electron microscope was smaller than that measured by DLS (128 nm) due to the nanogels' shrinkage under dry conditions.

X-ray photoelectron spectroscopy (XPS) analysis was performed to confirm the existence and valence states of the gold clusters in the mHA-GC hybrid nanogels. The XPS wide scan spectrum clearly showed the characteristic peaks of Au (4f) and S (2p) (Fig. 2C). As shown in Fig. 2D, the Au $4f_{7/2}$ binding energy (BE) of the hybrid nanogels is 84.1 eV, which falls in the middle between Au (0) BE (84 eV) of a metallic gold film and the Au(I) BE (86.0 eV) of gold thiolate, suggesting the coexistence of Au (0) and Au(I) in the clusters.[21] According to previous reports,[26] this observation revealed the contribution of the mHA-GC hybrid nanogels to the luminescence of the Au clusters due to the ligand–metal charge transfer and Au(I)–Au (I) interactions. In addition, the composition of the hybrid nanogels was determined by elemental analysis and inductively coupled plasma mass spectrometry (ICP-MS). The results revealed the high organic content of the sample (>81% wt.%) and an Au : S molar ratio of 1 : 3.5.

Fig. 2E shows the variation in the mean diameter and zeta potential of the mHA-GC hybrid nanogels at different pH values. The average size of the hybrid nanogels was almost invariant upon changing the medium pH, indicating the good stability of the hybrid nanogels. In contrast, the zeta potential of the hybrid nanogels decreased with the increasing pH of the medium. The zeta potential of these nanogels was −24 mV at pH = 3, while it became −33 mV at pH 7.4.

Optical properties of mHA-GC hybrid nanogels

The optical properties are an important function for gold cluster nanomaterials used as biological probes. The UV-vis absorption and photoluminescence spectra of the mHA-GC hybrid nanogels are shown in Fig. 3A. No surface plasma absorption was observed in the UV-vis spectrum of the hybrid nanogels, which was significantly different from the conventional larger Au nanoparticles. The absorption was observed between 400 nm and 600 nm, with a small peak centered near 528 nm. The photoluminescence (PL) spectrum showed the broad emission band of the mHA-GC hybrid nanogels with a center at 655 nm upon excitation at 500 nm. Bright photoluminescence was clearly observed from the hybrid nanogel solution under UV irradiation, as shown in the inset of Fig. 3A. Interestingly, an extending emission wavelength was observed in the near-infrared (NIR) region (700–800 nm), which was a suitable window for imaging deep tissues. The NIR fluorescence imaging can be applied to the real-time tracking of drug delivery *in vivo* and image-guided cancer surgery due to its decreased autofluorescence and low light scattering.[3,27,28] Thus, the broad emission band covering the red to near-infra-red region makes the mHA-GC hybrid nanogels useful for *in vitro* and *in vivo* imaging. The quantum yield of the mHA-GC hybrid nanogels was determined to be ~0.8%, using Rhodamine 6G (QY = 95% in ethanol) as the reference.

The disulfide bonds of the mHA-GC hybrid nanogels are sensitive to reductive microenvironments such as tumor cells with high glutathione concentration. In addition, GSH exhibits strong affinity to Au clusters due to the presence of thiolate and other active groups in its structure. Thus, excess GSH can potentially alter the photophysical properties of Au clusters.[22] In order to examine the photostability of the hybrid nanogels in physiological and bio-reductive environments, a photoluminescence experiment was performed. Fig. 3B shows the PL spectra of the mHA-GC hybrid nanogels incubated in PBS

buffer at various time points. It could be seen that the PL intensity of the mHA-GC hybrid nanogels was nearly invariable at 4 h, and only decreased 17.7% after 96 h. In contrast, the PL intensity of the mHA-GC hybrid nanogels increased when the hybrid nanogels were incubated in PBS buffer containing GSH, as shown in Fig. 3C and D. Moreover, increasing the concentration of GSH in PBS led to a significant enhancement of the PL intensity. It was interesting that the PL intensity of the mHA-GC hybrid nanogels incubated in PBS buffer with 10 mM GSH for 4 h increased up to 136%, and further increased by 37.2% at 96 h (Fig. 3D). In this case, the NIR emission intensity of the hybrid nanogels at 700 nm also increased to 114%, and further by 58.1% and 26.6%, corresponding to 4 h, 48 h and 96 h, respectively (Fig. 3E). The fluorescence enhancement of the hybrid nanogels after the addition of GSH may be attributed to the ligand exchange between GSH and the cystamine unit, and the ligand-to-metal charge transfer (LMCT) from the sulfur atom in thiolates to the Au atoms. Compared with cystamine, GSH contains more electron-rich groups, which has stronger charge donating capability to the metal core *via* Au–S bonds and thus leads to the fluorescence enhancement.[29,30] Therefore, the reduction-responsive light-emitting enhancement property of the mHA-GC hybrid nanogels makes them very promising for use as fluorescent platforms in biology.

Cellular uptake of the hybrid nanogels

As a theranostic system, the cellular uptake of the mHA-GC hybrid nanogels is important to evaluate the cytotoxicity and biological activity of chemotherapeutic formulations. Meanwhile, the inherent fluorescence characteristics of gold nanoclusters in the hybrid nanogels can be used to trace the cellular uptake behavior of the nanogels by using fluorescence imaging. Considering that CD44 is overexpressed in A549 cells and underexpressed in NIH3T3 cells, while CD168 is overexpressed in H22 cells,[17] these three kinds of cell lines were used for our study. Hence, after the mHA-GC hybrid nanogels were incubated with A549, H22 and NIH3T3 cells for 4 h at 37 °C and the nuclei were stained with Hoechst 33258, the cellular uptake of the hybrid nanogels was observed by CLSM. As shown in Fig. 4A and B, the red punctate fluorescence signals from the gold clusters of the nanogels were visible in the cytosol, indicating that the hybrid nanogels can be efficiently internalized by the A549 and H22 cells through the endocytosis pathway. In contrast, the fluorescence intensity of the hybrid nanogels in the NIH3T3 cells was so weak that the signal could be barely detected (Fig. 4C). To obtain a quantitative comparison, the cellular uptake of the mHA-GC hybrid nanogels in A549, H22 and NIH3T3 cells was further analyzed by flow cytometry (FCM). Fig. 4D shows that the cellular uptake by the A549 and H22 cells of the hybrid nanogels amounted to 2.0 and 1.8 times higher than that by the NIH3T3 cells, respectively. This result is consistent with that from the CLSM uptake assay, confirming that the specific receptors (such as CD44 or CD168) play a key role in cell recognition, binding and internalization. Hence, the mHA-GC hybrid nanogels have great cellular selectivity.

Real-time near-infrared fluorescence (NIRF) imaging *in vivo*

To investigate the distribution and tumor accumulation of the mHA-GC hybrid nanogels *in vivo* in real time, the noninvasive near-infrared fluorescence (NIRF) imaging technique was employed. Herein, the gold clusters in the hybrid nanogels showed a broader fluorescence-

emitting signal, making the hybrid nanogels visible in the NIR range *in vivo*. Fig. 5A shows the typical NIR fluorescence images of the H22 tumor-bearing mice at different times after tail vein injection of the hybrid nanogels. It was found that the strong fluorescence signals appeared in the liver at 1 and 2 h post-injection (p.i.), suggesting that a portion of the mHA-GC hybrid nanogels was rapidly recognized by the phagocyte and the reticuloendothelial system (RES). Meanwhile, it was noteworthy that the fluorescence signal appeared early in the tumor area at 1 h post-injection and further increased within 48 h, indicating that the hybrid nanogels can reach the tumor site quickly. Then, a slight decrease of the fluorescence intensity in the tumor area was observed from 72 to 96 h. This result reveals the fast accumulation of the hybrid nanogels at the tumor site due to the intrinsic EPR effect and the targeting action of hyaluronic acid toward the H22 tumor site. Quantitative data of the time-dependent fluorescence intensity were acquired by detecting the total photon counts at the tumor site and then normalized by the tumor area (Fig. 5B). The fluorescence intensity in the tumor region was already high at 1 h post-injection and then reached a maximum from the initial 48 h p.i., further indicating that the mHA-GC hybrid nanogels can accumulate in the tumor very quickly and the gold clusters can emit a strong NIR signal.

To further observe the accumulation of the nanogels in different organs, the mice were sacrificed at 96 h post-injection, and the *ex vivo* fluorescence images of the tumor tissue and major organs such as liver, heart, lungs, spleen and intestine were obtained. As shown in Fig. 5C, the relatively strong fluorescence signals can still be observed in the liver, spleen and tumor, indicating that the hybrid nanogels were mostly taken up by the liver, spleen and tumor, and had a long retention time in the tumor sites.

Redox responsiveness of the mHA-GC hybrid nanogels

The mHA-GC hybrid nanogels were expected to be stable in the circulation system and extracellular space, but disassemble in tumor cells. As mentioned above, the disulfide-containing hybrid nanogels were well sensitive to reductive molecules such as GSH. It has been reported that the intracellular GSH concentration (2–10 mM) is 100 to 1000 times higher than that in blood stream.[14] Moreover, the concentration of GSH in tumor cytosol was about 10-fold higher than in normal tissues.[25,31] Therefore, the reduction-responsive behaviors of the hybrid nanogels were examined in PBS with 0 and 10 mM GSH. The changes in the light scattering intensity and size of the nanogels with time were monitored by DLS, as shown in Fig. 6A. Upon incubation with 10 mM GSH, the size of the mHA-GC hybrid nanogels was slowly increased from 124 nm to about 168 nm. Apparently, this phenomenon was the result of the cleavage of the unbound disulfide bonds in the hybrid nanogels, leading to the disassembly of a large amount of the nanogels and swelling up of a few of the nanogels.[32] In comparison, the size of the nanogels was nearly unchanged in the absence of GSH. Thus, this result showed that the mHA-GC hybrid nanogels could be stable in the circulation and decrosslinked in the reductive cytoplasm, which was in favour of *in vivo* bioimaging and intracellular delivery of anticancer drugs.

DOX loading and drug release *in vitro*

Considering that there were abundant carboxyl groups in the hyaluronic acid molecule, the mHA-GC hybrid nanogels seem to be appropriate to load DOX since the DOX molecule has

an amino group. DOX was loaded into the hybrid nanogels by an incubation method exploiting the electrostatic interactions between the positively charged DOX molecules and negatively charged hybrid nanogels. Accordingly, we were pleased to accomplish a drug loading content of 16% with an encapsulation efficiency of 96%. After drug loading, the average diameter of the DOX-loaded hybrid nanogels increased from 128 nm to 143 nm as measured by DLS.

Next the release profiles of DOX from the mHA-GC hybrid nanogels were measured using a UV-Vis spectrometer. Fig. 6B shows the release profiles of DOX from the hybrid nanogels in different pH media with or without 10 mM GSH at 37 °C. In the absence of GSH, only about 28% of the loaded DOX was released within 144 h at pH 7.4, suggesting that the DOX release from the hybrid nanogels in neutral medium is significantly suppressed. With the decrease of the medium's pH, the amount of cumulative release of the drug from the hybrid nanogels increased dramatically. At pH of 6.0 and 5.0, the release amounts of DOX from the hybrid nanogels were *ca*. 42% and 50% within 144 h, respectively, indicating that the release of DOX from the hybrid nanogels speeds up with the decrease in the pH value of the medium. We ascribed these results to the weakening of the electrostatic interactions between the HA and DOX, which causes the leakage of DOX from the hybrid nanogel matrix at a low pH value. On the other hand, in the presence of 10 mM GSH, the release amounts of DOX increased sharply to about 41%, 61% and 81% at pH 7.4, 6.0 and 5.0, respectively, within 144 h. This result demonstrates that the DOX release from the hybrid nanogels is accelerated by acidic and reductive environments.

In vitro cytotoxicity of the DOX-loaded hybrid nanogels

To verify the pharmacological activity of the DOX-loaded mHA-GC hybrid nanogels and the potential toxicity of the blank hybrid nanogels, the *in vitro* cytotoxicity of the drug-loaded and blank hybrid nanogels was examined using MTT assays. The cell viability of A549, H22 and NIH3T3 cells after 24 h of incubation with free DOX and the drug-loaded nanogels was examined, as presented in Fig. 7A–C. A dose dependent cytotoxicity was observed for both free DOX and the DOX-loaded hybrid nanogels. After incubation with the DOX-loaded hybrid nanogels at a concentration of 32 μg mL^{-1} DOX, 83% of A549, 64% of H22 and 46% of NIH3T3 cell proliferations were inhibited. The difference in the cytotoxicity of these cell lines might be attributed to their different sensitivity to DOX and the effect of the overexpressed receptor mediated cellular uptake. Moreover, the cytotoxicity of the drug-loaded nanogels against the A549 cells was higher than that of free DOX at a high DOX concentration.

In comparison, the cell viabilities of the blank hybrid nanogels were over 90% at all of the used concentrations, demonstrating the good cytocompatibility of the mHA-GC hybrid nanogels (Fig. 7D). The results indicate that DOX can still retain its pharmacological activity when encapsulated into the hybrid nanogels, and the hybrid nanogels have an enhanced anticancer activity with receptor targeting.

Cell apoptosis and proliferation tests

DOX is a chemotherapeutic drug that is known to interact with DNA and induces apoptosis of tumor cells. Thus, to investigate the therapeutic effects of the DOX-loaded mHA-GC hybrid nanogels, the extent of apoptosis and cell proliferation induced in the tumor tissue were determined using TUNEL staining and PCNA staining on day 8 post-injection (for the group with multiple doses, the day after the last injection), respectively.[33] The cells in brown color correspond to the apoptotic cells in the TUNEL test, while they represent the proliferating cells in the PCNA test. From Fig. 8A, it could be seen that the apoptotic degree of the cells was significantly low and negligible in the tumor tissues of the group receiving saline and the blank hybrid nanogels. On the other hand, both free DOX and the hybrid nanogels with an equivalent dose of DOX caused apoptosis in the tumor tissue. The tumor tissue treated with multiple doses of the DOX-loaded mHA-GC hybrid nanogels showed the highest degree of cell apoptosis (*ca.* 43.9%) compared to the groups of free DOX (19%) and a single dose (23.7%), indicating that multiple dose injection induces the highest degree of apoptosis of tumor cells (Fig. 8B). As expected, the percentage of the PCNA positive (proliferating) cells was significantly lower in the group which received a multiple dose trial compared with the tumors of the other groups (Fig. 8A and C). In contrast, the percentages of the proliferating cells in the tumor of the groups receiving saline and the blank hybrid nanogel treatment were above 65%, indicating that the majority of the cells are proliferating. All of the above results demonstrate that the DOX-loaded mHA-GC hybrid nanogels have a superior anticancer effect. It can also be confirmed that the multiple dose treatment using the hybrid nanogels results in a continuous and efficient delivery of DOX to the tumor region and high pharmacological efficacy.

Conclusions

In summary, a type of mHA-GC hybrid nanogel was designed and prepared, which integrated bioimaging, *in vivo* tracing, microenvironment-responsive drug-release and tumor targeting functions into a single nanocomposite. It was found that the obtained hybrid nanogels possessed intense red–NIR fluorescence and their emission intensity was significantly enhanced (up to 136%) by GSH induction, which enabled us to observe the cellular uptake and *in vivo* transport of the hybrid nanogels in a label-free fashion. The hybrid nanogels had a stable particle structure but were disassembled in reductive environments, which facilitated the selective release of the DOX loaded nanogels. Also, the evaluation of *in vitro* cellular uptake and cytotoxicity showed that the DOX-loaded mHA-GC hybrid nanogels had a noteworthy affinity to the HA-specific receptor overexpressed in cancer cells and higher cytotoxicity than free DOX. From the NIRF imaging, it was found that the hybrid nanogels could reach the tumor site quickly and displayed a continuous accumulation in the tumor site at the first 48 h and remained there for 96 h, which demonstrates the prominent tumor targeting ability and remarkable EPR effect of the mHA-GC hybrid nanogels. The tumor cell apoptosis examinations revealed that the DOX-loaded hybrid nanogels had significantly superior *in vivo* antitumor efficiency in H22 tumor-bearing mice as compared to free DOX. Thus, the chemical design of the hybrid nanogels provides an attractive strategy to realize active tumor targeting and stimulation of intratumoral drug release, thereby improving cancer theranostic efficacy.

Acknowledgements

This work was supported by the National Key R&D Program of China (2017YFA0701301 and 2017YFA0205401), Natural Science Foundation of China (no. 51303003, 21720102005 and 51690153), and Anhui Higher Education Exchange Program for Young Talents (no. gxfx2017044). This work was also supported in part by the University of Wisconsin-Madison and NIH (P30CA014520).

Notes and references

1. Wang J, Liu J, Liu Y, Wang L, Cao M, Ji Y, Wu X, Xu Y,Chen C and Zhao Y, Adv. Mater, 2016, 28, 8950–8958. [PubMed: 27562240]
2. Cheng P and Pu K, ACS Appl. Mater. Interfaces, 2020, 12, 5286–5299.
3. Shi B, Du X, Chen J, Fu L, Morsch M, Lee A, Liu Y,Cole N and Chung R, Small, 2017, 13, 1603966.
4. Minchinton AI and Tannock IF, Nat. Rev. Cancer, 2006, 6, 583–592. [PubMed: 16862189]
5. Blanco E, Shen H and Ferrari M, Nat. Biotechnol, 2015, 33, 941–951. [PubMed: 26348965]
6. Tapeinos C, Larrañaga A, Tomatis F, Bizeau J, Marino A,Battaglini M, Pandit A and Ciofani G, Adv. Funct. Mater, 2019, 30, 1906283.
7. Chen W, Zhou S, Ge L, Wu W and Jiang X, Biomacromolecules, 2018, 19, 1732–1745. [PubMed: 29690764]
8. Chen H, Gu Z, An H, Chen X, Jiang X, Liu Z, Pang D,Tan W, Zhang X, Zhao Y, et al., Sci. China: Chem, 2018, 61, 1503–1552.
9. Wang X, Wang X, Jin S, Muhammad N and Guo Z, Chem. Rev, 2019, 119, 1138–1192. [PubMed: 30299085]
10. Zhang Y, Yang D, Chen H, Lim W, Phua F,An G, Yang P and Zhao Y, Biomaterials, 2018, 163, 14–24. [PubMed: 29452945]
11. Li Y, Lin J, Wang P, Luo Q, Lin H, Zhang Y,Hou Z, Liu J and Liu X, ACS Nano, 2019, 13, 12912–12928. [PubMed: 31651142]
12. Hayashi K, Maruhashi T, Nakamura M, Sakamoto W and Yogo T, Adv. Funct. Mater, 2016, 26, 8613–8622.
13. Xia J, Du Y, Huang L, Chaurasiya B, Tu J, Webster TJ and Sun C, Nanomedicine, 2018, 14, 713–723. [PubMed: 29317344]
14. Cheng R, Feng F, Meng F, Deng C, Feijen J and Zhong Z, J. Controlled Release, 2011, 152, 2–12.
15. Li N, Chen Y, Zhang Y, Yang Y, Su Y, Chen J and Liu Y, Sci. Rep, 2014, 4, 4164. [PubMed: 24566666]
16. Li J, Huo M, Wang J, Zhou J, Mohammad J, Zhang Y,Zhu Q, Waddad A and Zhang Q, Biomaterials, 2012, 33, 2310–2320. [PubMed: 22166223]
17. Yang C, Wang X, Yao X, Zhang Y, Wu W and Jiang X,J. Controlled Release, 2015, 205, 206–217.
18. Kim H, Shin M, Han S, Kwon W and Hahn S, Biomacromolecules, 2019, 20, 2889–2903. [PubMed: 31251565]
19. He Y, Cheng G, Xie L, Nie Y, He B and Gu Z, Biomaterials, 2013, 34, 1235–1245. [PubMed: 23127334]
20. Tripodo G, Trapani A, Torre M, Giammona G, Trapani G and Mandracchia D, Eur. J. Pharm. Biopharm, 2015, 97, 400–416. [PubMed: 26614559]
21. Shang L, Azadfar N, Stockmar F, Send W, Trouillet V,Bruns M, Gerthsen D and Nienhaus GU, Small, 2011, 7, 2614–2620. [PubMed: 21809441]
22. Aldeek F, Muhammed MAH, Palui G, Zhan N and Mattoussi H, ACS Nano, 2013, 7, 2509–2521. [PubMed: 23394608]
23. Chen L, Wang C, Yuan Z and Chang H, Anal. Chem, 2015, 87, 216–229. [PubMed: 25275676]
24. Yahia-Ammar A, Sierra D, Mérola F, Hildebrandt N and Guével X, ACS Nano, 2016, 10, 2591–2599. [PubMed: 26845515]
25. Qian H, Wang X, Yuan K, Xie C, Wu W, Jiang X and Hu L, Biomater. Sci, 2014, 2, 220–232. [PubMed: 32481882]

26. Wu Z and Jin R, Nano Lett, 2010, 10, 2568–2573. [PubMed: 20550101]
27. Ni X, Zhang X, Duan X, Zheng H, Xue X and Ding D, Nano Lett, 2019, 19, 318–330. [PubMed: 30556699]
28. Chen C, Ni X, Tian H, Liu Q, Guo D and Ding D, Angew. Chem., Int. Ed, 2020, 59, 10008–10012.
29. Guével XL, Perrino MP, Fernandez TD, Palomares F,Torres M, Blanca M, Rojo J and Mayorga C, ACS Appl. Mater. Interfaces, 2015, 7, 20945–20956. [PubMed: 26329370]
30. Zhang X, Wu F, Liu P, Gu N and Chen Z, Small, 2014, 10, 5170–5177. [PubMed: 25111498]
31. Kuppusamy P, Li H, Hangovan G, Cardounel AJ,Zweier JL, Yamada K, Krishna MC and Mitchell JB, Cancer Res, 2002, 62, 307–312. [PubMed: 11782393]
32. Jiang Z, Zhu Z, Liu C, Hu Y, Wu W and Jiang X, Polymer, 2008, 49, 5513–5519.
33. Okino H, Maeyama R, Manabe T, Matsuda T and Tanaka M, Clin. Cancer Res, 2003, 9, 5786–5793. [PubMed: 14654564]

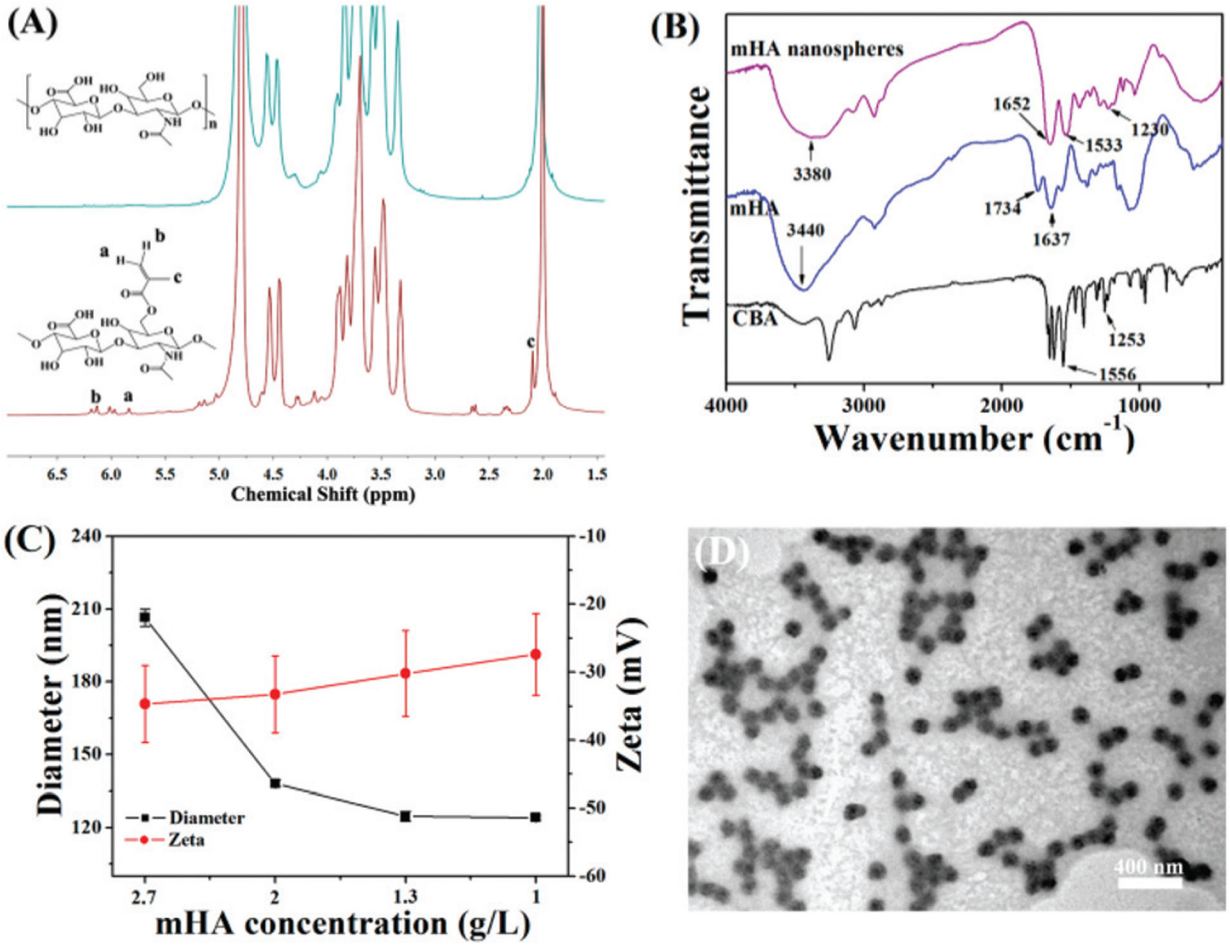

Fig. 1.

(A) ^{1}H NMR spectra of HA (up) and mHA (bottom). (B) FT-IR spectra of mHA, CBA and mHA nanogels. (C) Diameter and zeta potential of mHA nanogels obtained with different concentrations of mHA (data are represented as means ± SD, $n = 3$); (D) TEM image of the mHA nanogels.

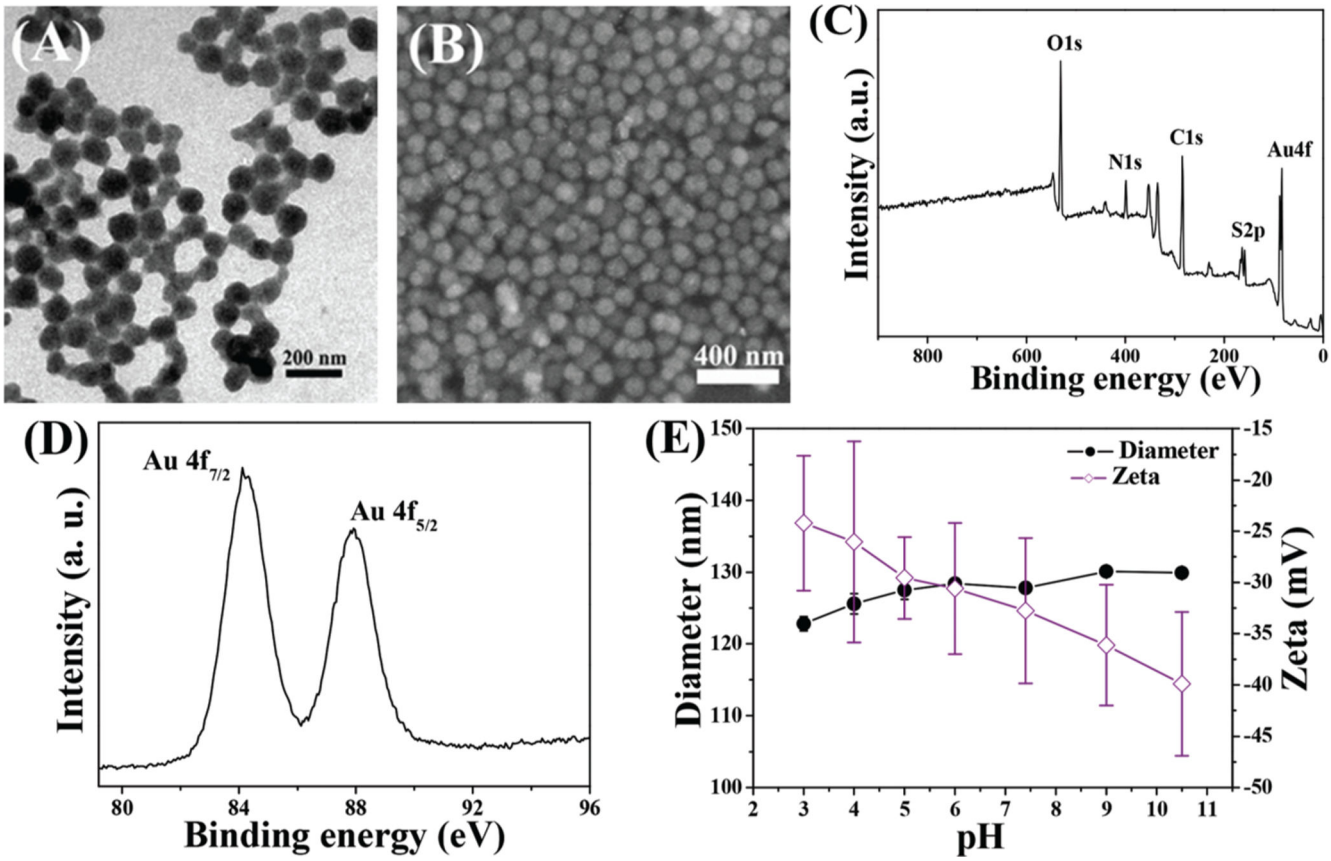

Fig. 2.

(A) TEM and (B) SEM images of the mHA-GC hybrid nanogels. The typical XPS wide scan spectrum (C) and Au 4f spectrum (D) for mHA-GC hybrid nanogels. (E) Influence of pH on the hydrodynamic diameter and zeta potential of mHA-GC hybrid nanogels. Data are expressed as means ± SD (n = 3).

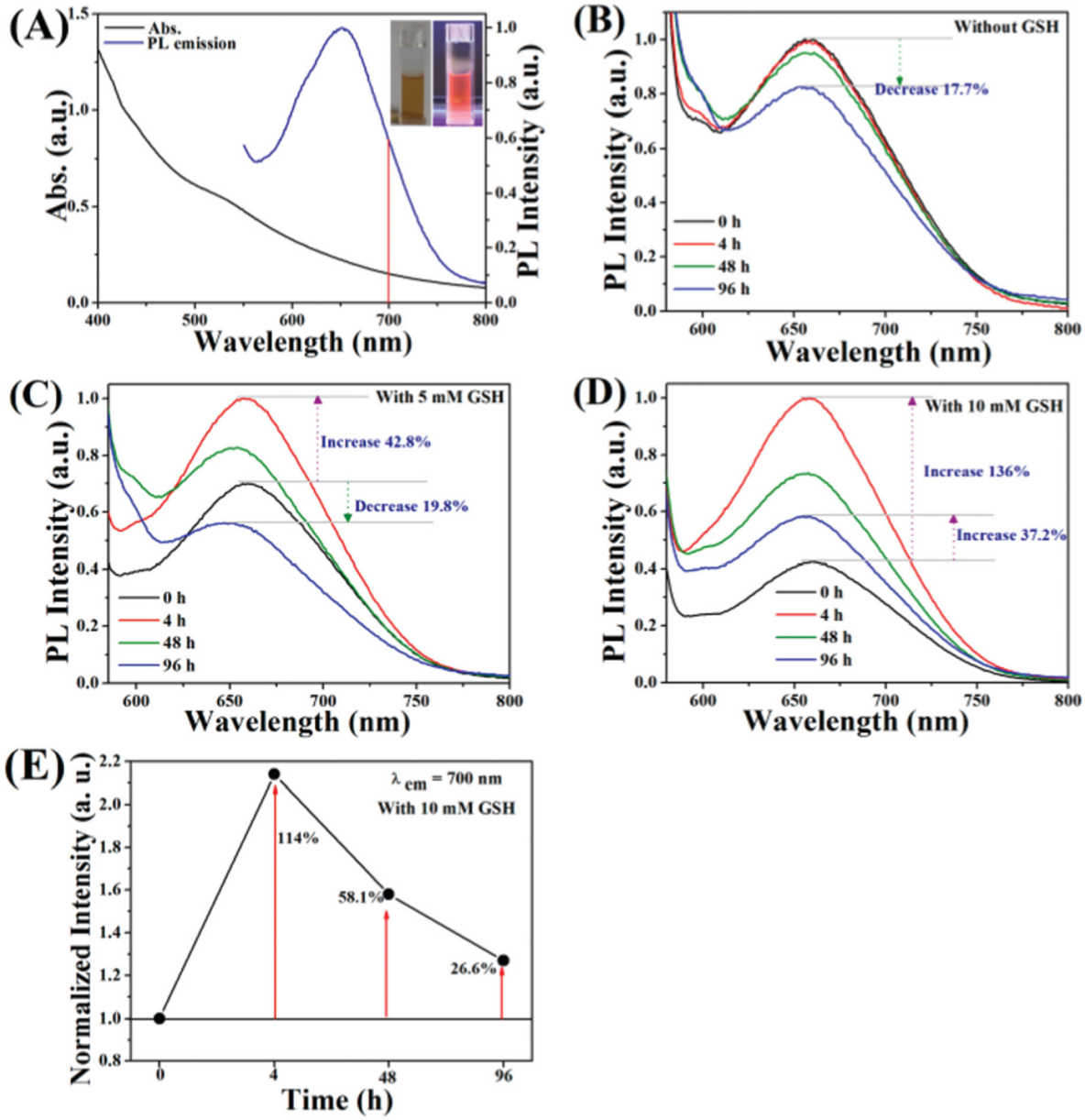

Fig. 3.

(A) UV-vis absorption and PL emission spectra of mHA-GC hybrid nanogels excited at 500 nm. Inset: photographs of the hybrid nanogel aqueous solution under visible (left) and UV light irradiation (right). PL spectra of mHA-GC hybrid nanogels in PBS buffer (B), PBS buffer containing 5 mM GSH (C) and PBS buffer containing 10 mM GSH (D) at 37 °C for various time periods, λ_{ex} = 550 nm. (E) The PL emission enhancement at 700 nm of hybrid nanogels in PBS buffer containing 10 mM GSH at different times and 37 °C. The emission intensities measured at various time points were normalized to the initial intensity.

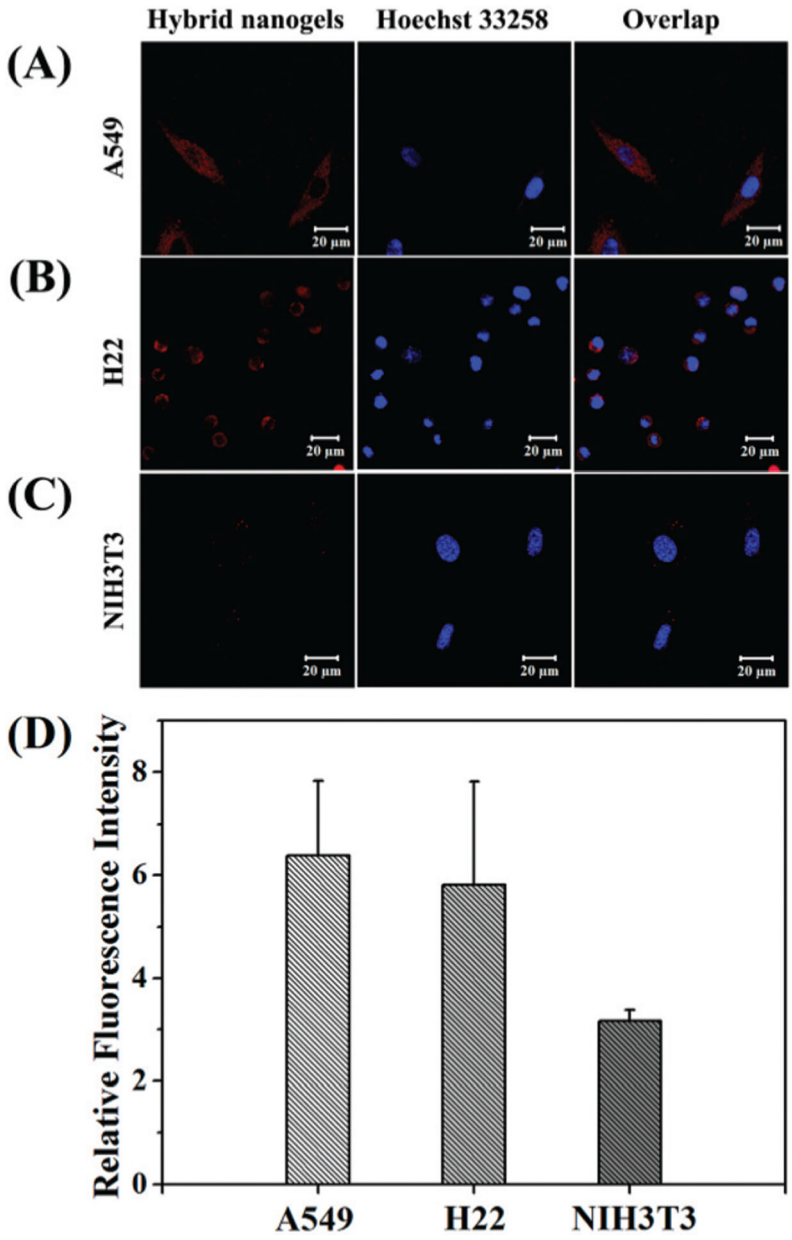

Fig. 4.

Confocal images of (A) A549, (B) H22 and (C) NIH3T3 cells after incubation with mHA-GC hybrid nanogels (red). The nuclei were dyed with Hoechst 33258 (blue). (D) Flow cytometry analysis of mHA-GC hybrid nanogels incubated with A549, H22 and NIH3T3 cells compared with the control respectively (4 h of incubation at 37 °C); data as mean values ± SD (n = 3).

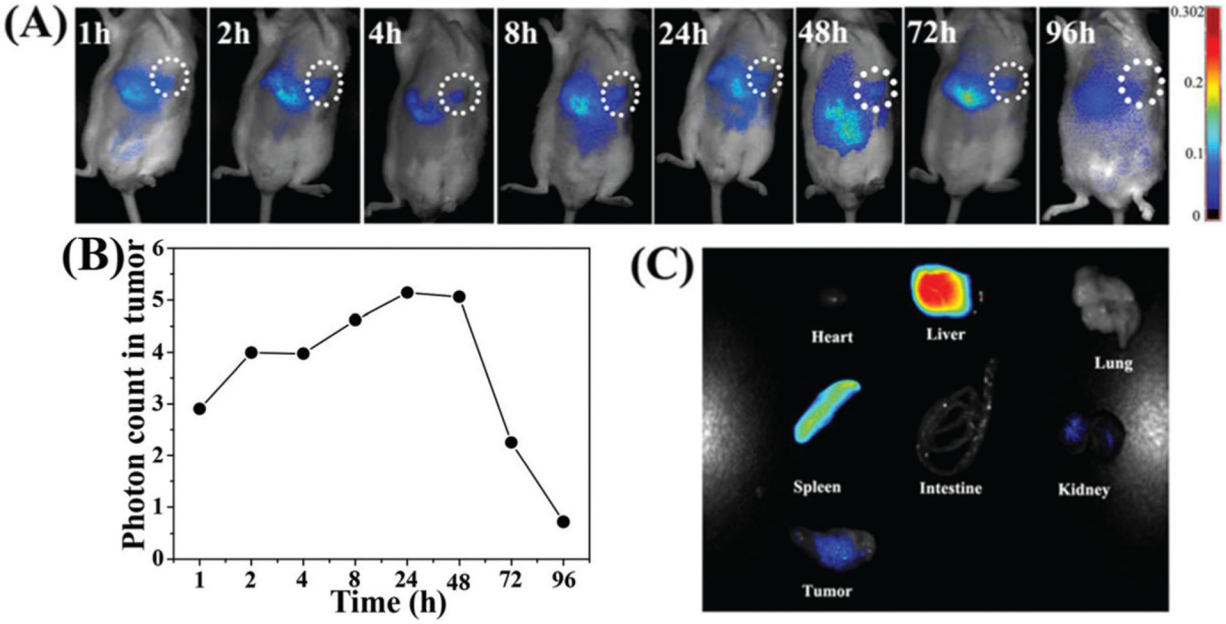

Fig. 5.

(A) NIR fluorescence images of the H22 tumor-bearing mouse after the intravenous injection of mHA-GC hybrid nanogels. Tumor areas are surrounded with the dashed circle. (B) The time dependent fluorescence intensity of the tumor region. (C) The NIR fluorescence images of the major organs and tumor at 96 h post-injection.

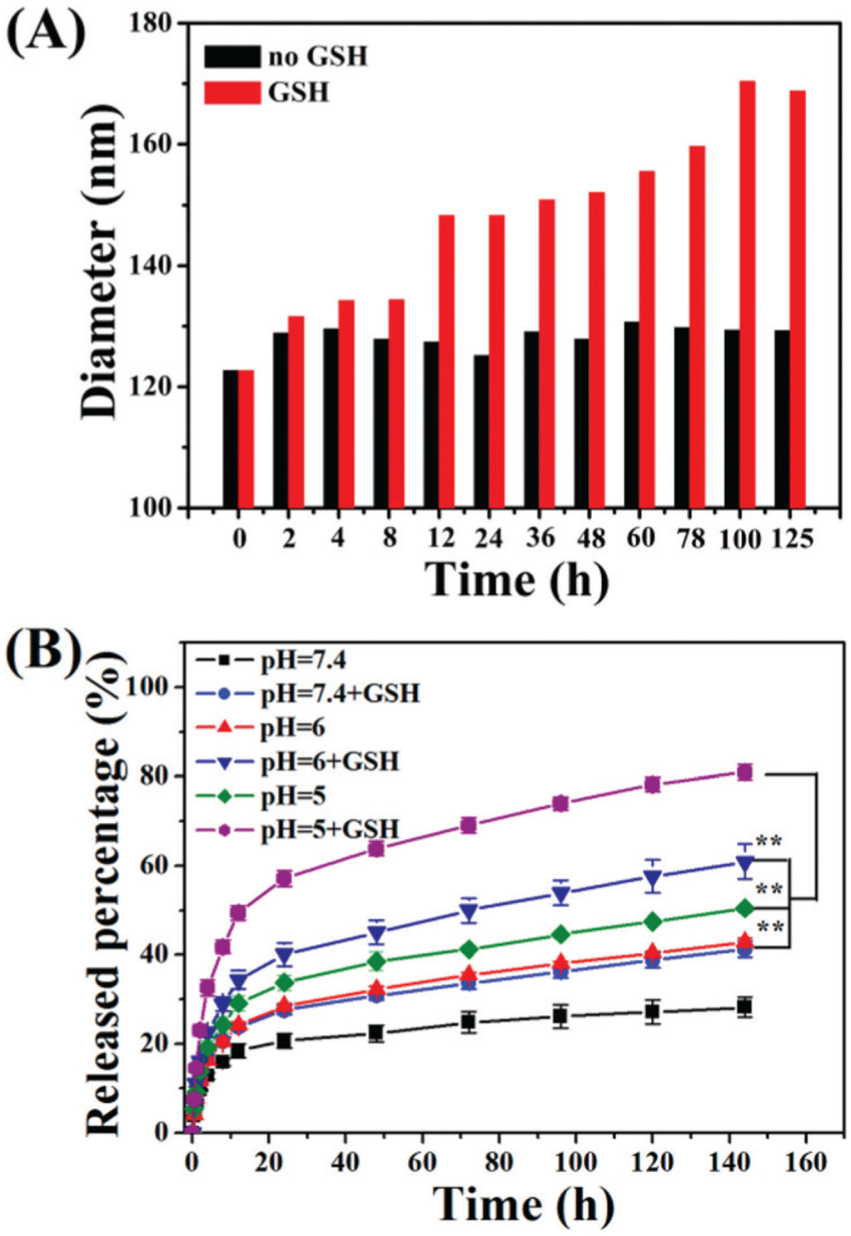

Fig. 6.

(A) The diameter of mHA-GC hybrid nanogels at 37 °C in the absence or presence of 10 mM GSH, respectively against time. (B) *In vitro* DOX release profiles of the hybrid nanogels in PBS (pH = 5, 6, 7.4, 10 mM) at 37 °C with or without GSH (10 mM). The results represent the means ± SD ($n = 3$). ** represents $P < 0.01$.

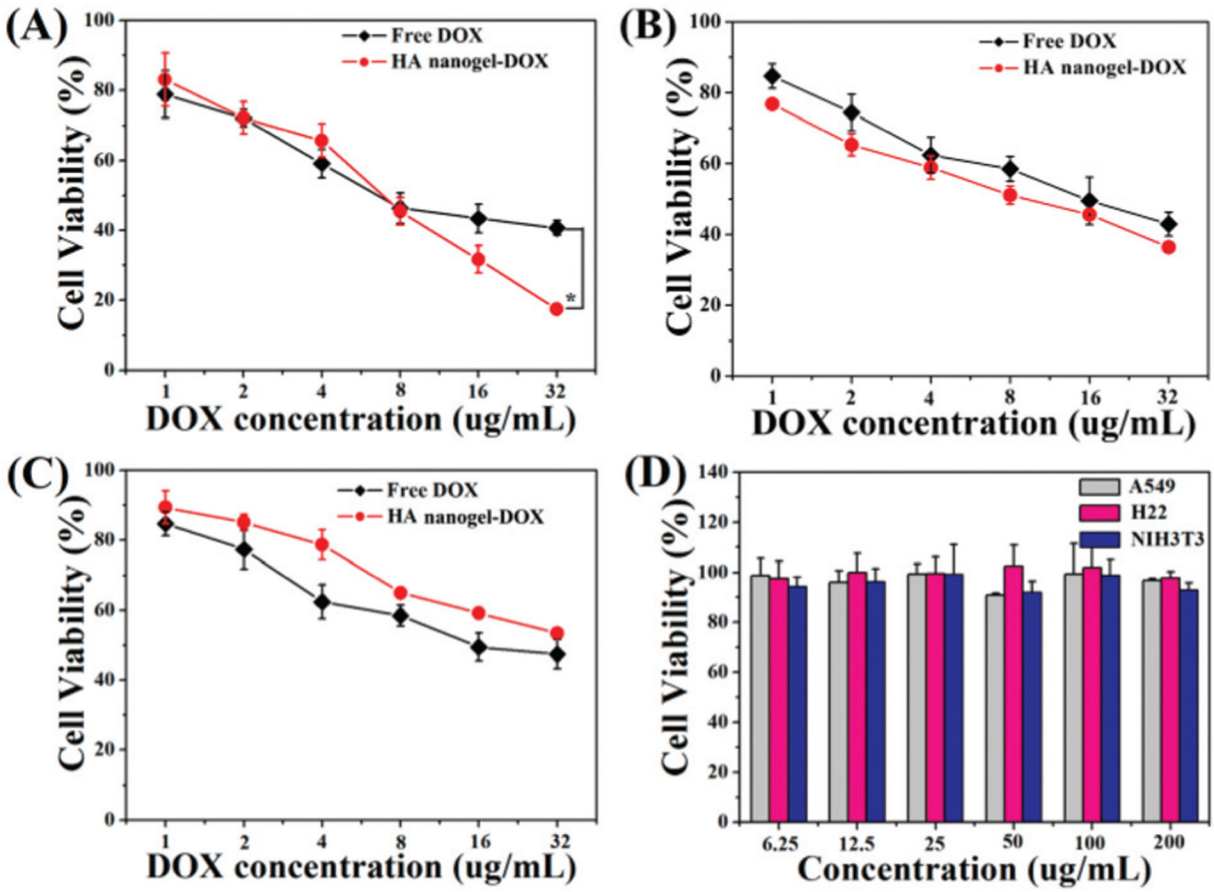

Fig. 7.

In vitro cytotoxicity of DOX-loaded hybrid nanogels in comparison with free DOX against (A) A549, (B) H22 and (C) NIH3T3 cell lines after 24 h of incubation (* represents $P < 0.05$). (D) Viability of A549, H22 and NIH3T3 cell lines after incubation with mHA-GC hybrid nanogels for 24 h.

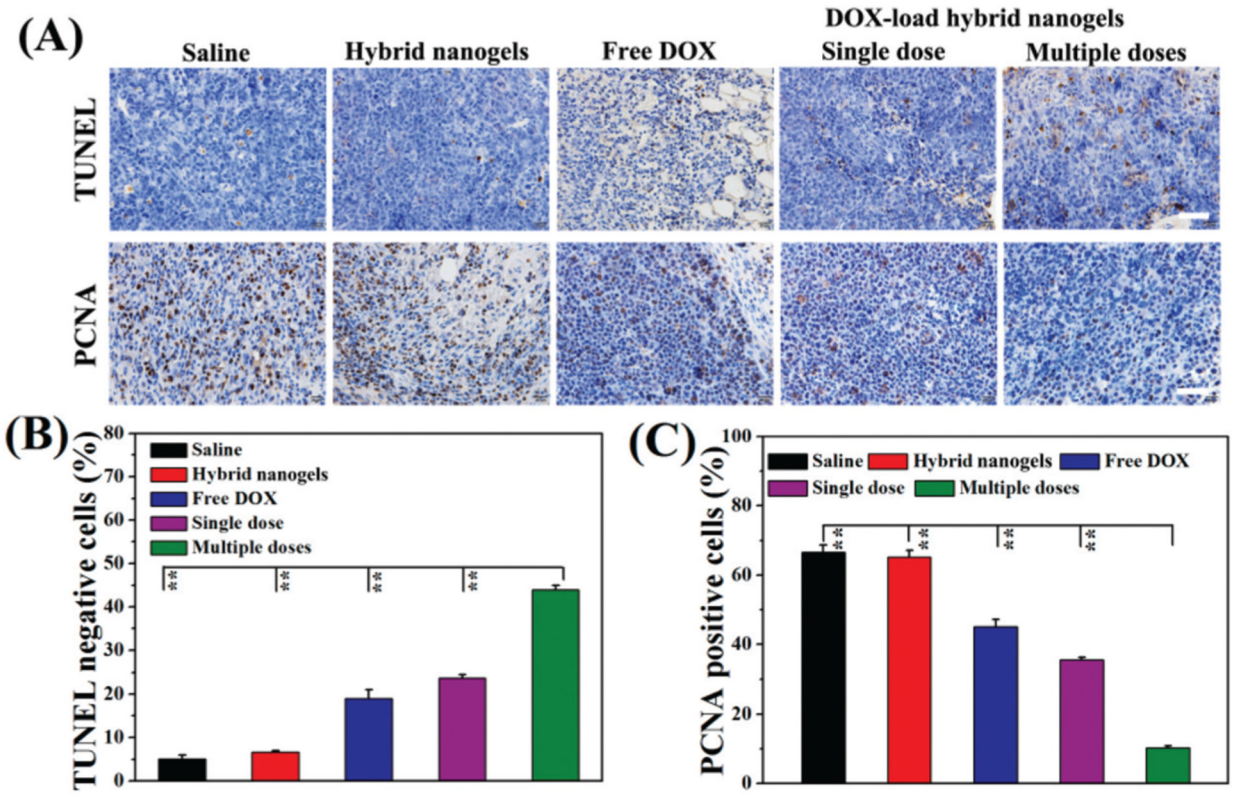

Fig. 8.

(A) The TUNEL and PCNA observations of H22 tumors obtained from the mice receiving various treatments. The scale bar in each figure is 50 μm. The comparison of apoptotic cells (B) and proliferating cells (C) in H22 tumors obtained from the mice (** represents $P < 0.01$).

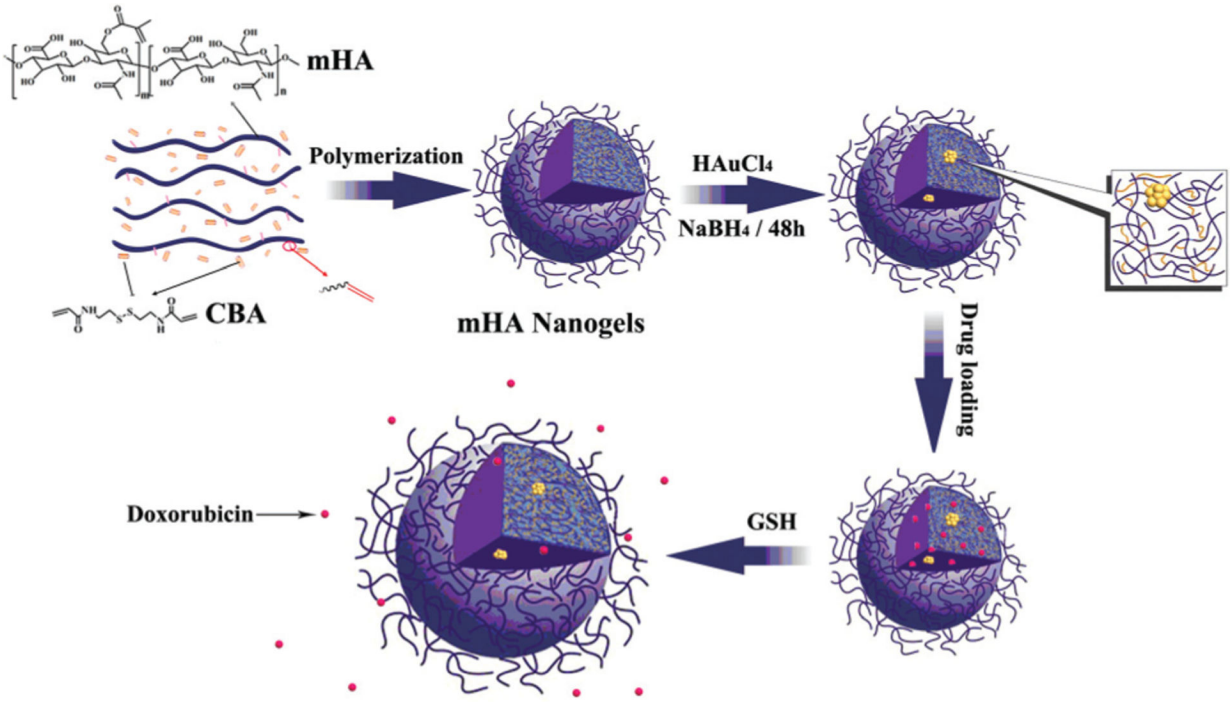

Scheme 1.

Schematic illustration of the synthesis of mHA-GC hybrid nanogels and release of the drug triggered by GSH.